SCIENTIFIC
REPORTS
natureresearch

Check for updates

OPEN

Femtosecond time-evolution of mid-infrared spectral line shapes of Dirac fermions in topological insulators

Tien-Tien Yeh[1,2 ✉], Chien-Ming Tu[1], Wen-Hao Lin[1], Cheng-Maw Cheng[2], Wen-Yen Tzeng[1], Chen-Yu Chang[1], Hideto Shirai[3], Takao Fuji[3,4], Raman Sankar[5,6], Fang-Cheng Chou[2,6], Marin M. Gospodinov[7], Takayoshi Kobayashi[1,8] & Chih-Wei Luo[1,9,10 ✉]

Mid-infrared (MIR) light sources have much potential in the study of Dirac-fermions (DFs) in graphene and topological insulators (TIs) because they have a low photon energy. However, the topological surface state transitions (SSTs) in Dirac cones are veiled by the free carrier absorption (FCA) with same spectral line shape that is always seen in static MIR spectra. Therefore, it is difficult to distinguish the SST from the FCA, especially in TIs. Here, we disclose the abnormal MIR spectrum feature of transient reflectivity changes ($\Delta R/R$) for the non-equilibrium states in TIs, and further distinguish FCA and spin-momentum locked SST using time-resolved and linearly polarized ultra-broadband MIR spectroscopy with no environmental perturbation. Although both effects produce similar features in the reflection spectra, they produce completely different variations in the $\Delta R/R$ to show their intrinsic ultrafast dynamics.

Time-resolved spectroscopy is important in various fields, such as determining the exotic carrier dynamics of TIs[1–7]. The photon energy (~100 meV) of a MIR is less than the bulk band gap of TIs and has a very different energy to the resonance energy of phonon absorptions. Therefore, MIR light sources are eminently suited to the study of SSTs in topological surface states (TSSs). The existing literature[8–22] reports the existence of a spectral line shape in the MIR region but there is no clear consensus. The explanation for FCA based on the Drude model has been adapted[11,12,17], but some studies give conflicting results[14,18] with considering more resonance factors. SSTs have also been reported[8–22] but these studies do not clarify the absorption mechanisms for SSTs and FCA using static MIR spectroscopic techniques.

This study unambiguously demonstrates the time evolution of MIR spectral line shapes in TIs using an optical pump and ultra-broadband MIR probe spectroscopy[23]. The MIR probe-pulses with a supercontinuum of 200–5000 cm^{-1} (or 25–620 meV) and a pulse width of 8.2 fs are generated using four-wave different-frequency generation (DFG) in nitrogen gas. *This novel spectroscopy technique has the advantages of a wide bandwidth for standard Fourier-transform-infrared spectroscopy (FTIR)[24] and it allows femtosecond time-resolution by generating ultrashort pulses from nonlinear crystals using DFG.* Two types of TI crystals are used for the experiments in this study. One is n-type Bi$_2$Te$_2$Se with a bulk/surface carrier concentration of 12.5×10^{18} cm^{-3}/5.5×10^{12} cm^{-2} (see S1 in Supplementary information), which is a bulk-conduction-electron-rich crystal. The other is p-type Sb$_2$TeSe$_2$ with a bulk/surface carrier concentration of 4.8×10^{18} cm^{-3}/2.2×10^{12} cm^{-2} (see S1 in Supplementary

[1]Department of Electrophysics, National Chiao Tung University, Hsinchu, Taiwan. [2]National Synchrotron Radiation Research Center, Hsinchu, 30076, Taiwan. [3]Institute for Molecular Science, 38 Nishigonaka, Myodaiji, Okazaki, 444-8585, Japan. [4]Toyota Technological Institute, 2-12-1 Hisakata, Tempaku-ku, Nagoya, 468-8511, Japan. [5]Institute of Physics, Academia Sinica, Nankang, Taipei, R.O.C, 11529, Taiwan. [6]Center for Condensed Matter Sciences, National Taiwan University, Taipei, 10617, Taiwan. [7]Institute of Solid State Physics, Bulgarian Academy of Sciences, 1784, Sofia, EU, Bulgaria. [8]Brain science Inspired Life Support Research Center, The University of Electro-Communications, 1-5 1 Chofugaoka, Chofu, Tokyo, 182-8585, Japan. [9]Taiwan Consortium of Emergent Crystalline Materials (TCECM), Ministry of Science and Technology, Taipei, Taiwan. [10]Center for Emergent Functional Matter Science, National Chiao Tung University, Hsinchu, 30010, Taiwan. ✉e-mail: jiljiljilji@gmail.com; cwluo@mail.nctu.edu.tw
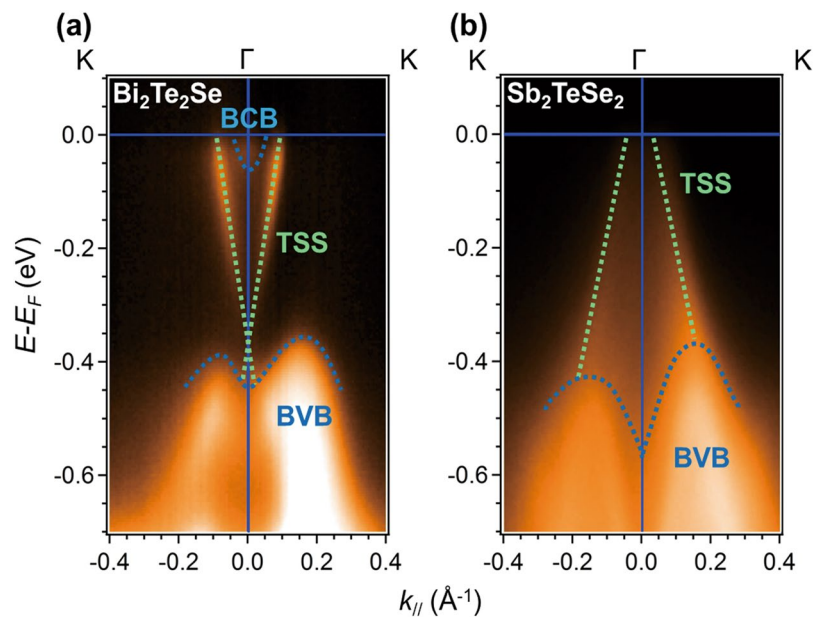
1

Figure 1. The angle resolved photoemission spectroscopy (ARPES) images of Bi_2Te_2Se and Sb_2TeSe_2 single crystals: (**a**) The ARPES image of a Bi_2Te_2Se single crystal measured with 22 eV photon energy. (**b**) The ARPES image of a Sb_2TeSe_2 single crystal measured with 24 eV photon energy. All single crystals were the same pieces as those used in ultrafast experiments for the consistency of all measurements. The single crystals were *in-situ* cleaved under a base pressure 5.1×10^{-11} torr at 85 K just before measurements. ARPES experiment was conducted National Synchrotron Radiation Research Center in Taiwan using BL21B1 beamline. The photoemission spectra were recorded with a Scienta R4000 hemispherical analyzer. The polarization vector was always in the angular dispersion plane. The overall energy resolution is about 12 meV. The green dash lines represent as the TSS of crystals, and the blue dash lines show the bulk-conduction-band (BCB) and bulk-valance-band (BVB). The Dirac point in Sb_2TeSe_2 was estimated at 189 meV above the Fermi level (see S1 in Supplementary information). A notable difference of band structure exists between Bi_2Te_2Se and Sb_2TeSe_2, the Dirac point of Bi_2Te_2Se is embedded in the BVB. In contrast to Bi_2Te_2Se, Sb_2TeSe_2 has an isolated Dirac cone and surface carriers cannot be scattered easily by bulk carriers. This difference in their band structure makes a significant difference in optical measurement results.

information), which features a higher ratio of surface to bulk carrier concentration. Figure 1 shows the clear presence of a bulk-conduction band (BCB) in Bi_2Te_2Se, but not in Sb_2TeSe_2.

Results

Ultra-broadband MIR $\Delta R/R$ spectra of FCA and SSTs in topological insulators.

The typical ultra-broadband MIR $\Delta R/R$ spectra for Bi_2Te_2Se and Sb_2TeSe_2 are respectively shown in Fig. 2a,b. These two spectra are significantly different. Along the wavenumber axis, there is a positive change in the lower frequency region and a negative change in the high frequency region, which indicates a blue-shift in the plasma edge for Bi_2Te_2Se after pumping (see Fig. 2c). The zero-crossing line, $L_{0,X}$ (dashed line), in Fig. 2a also shows a rapid blue-shift at the beginning of the delay time and then slowly (>50 ps) returns to the original position. However, the value of $\Delta R/R$ for Sb_2TeSe_2 shows a red-shift in the plasma edge after pumping. It is worthy of note that the zero-crossing line, $L_{0,X}$ (dashed line) in Fig. 2b is red-shifted until ~2 ps and then returns to the original position at ~6 ps, which is much faster than the change for Bi_2Te_2Se. Generally, there is a blue-shift in the plasma edge because there is an increase in the carrier concentration[25], which is explained by the Drude model. The red-shift in the $\Delta R/R$ spectrum of Sb_2TeSe_2 until ~2 ps is not explained by the Drude model because there is a decrease in the carrier concentration after pumping. It is found that the SST model using Kubo formula[20] (SST-Kubo model), which has been successfully used to explain the transitions of Dirac cone in graphene[20], explains the novel phenomena that are observed in p-type Sb_2TeSe_2.

By comparing the band mapping results of Bi_2Te_2Se and Sb_2TeSe_2 in Fig. 1, a notable difference between Bi_2Te_2Se and Sb_2TeSe_2 can be found that the Dirac point of Bi_2Te_2Se is embedded in the BVB. The surface carriers cannot avoid scattering from bulk carriers, and the major change of optical property might be dominated by bulk carrier. In contrast to Bi_2Te_2Se, Sb_2TeSe_2 has an isolated Dirac cone and thus the surface carriers cannot be scattered easily by bulk carriers, that is why the SST is a major factor in Sb_2TeSe_2. Besides, the difference between bulk FCA of the Bi_2Te_2Se and SST of Sb_2TeSe_2 could be attributed to the intrinsic responses with a 1.55-eV excitation. As the schematics of Fig. 4e,j, the final and initial states of excitation process are different. The photoexcited carriers of the former are excited from the valence band maximum to the second conduction band[2,4,26], which is far from the Fermi level. For the latter case, the photoexcited carriers are excited from a deep valance band to the states near Fermi level consisted of an isolated Dirac cone[5]. Therefore, the MIR probe beam tends to detect the free carriers of conduction band in Bi_2Te_2Se, and the SST near Fermi level in Sb_2TeSe_2.
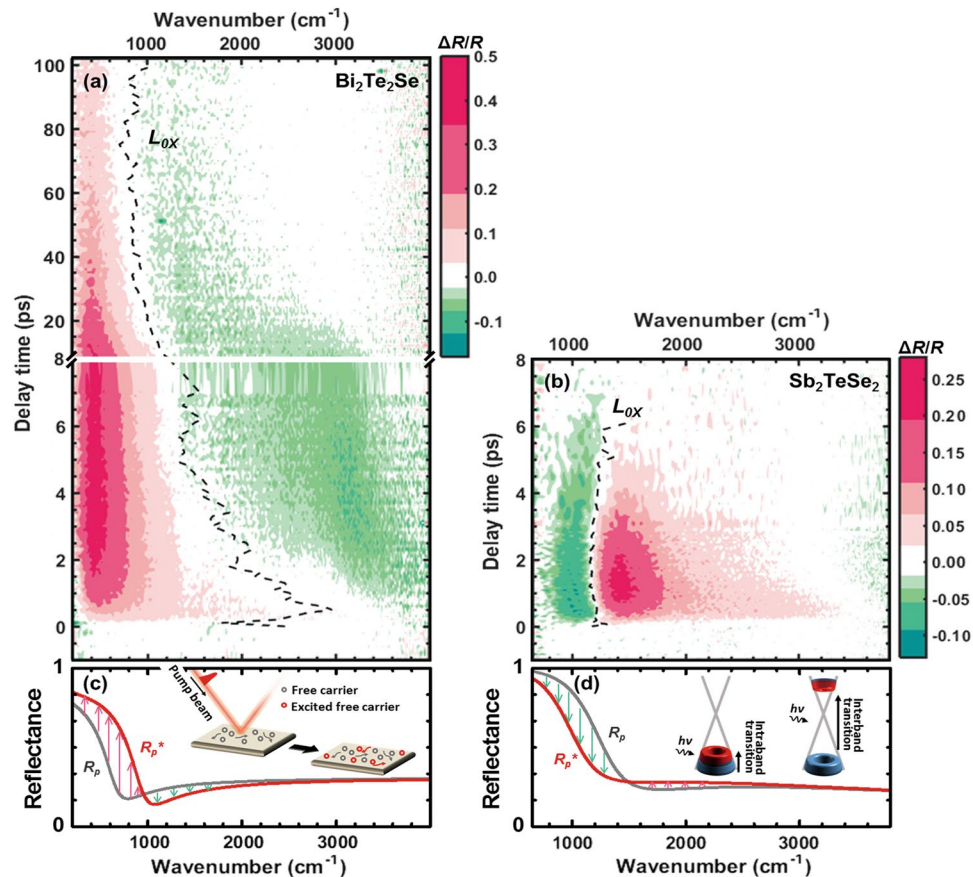
Figure 2. The time-resolved ultra-broadband MIR $\Delta R/R$ spectra for Bi_2Te_2Se and Sb_2TeSe_2 single crystals and the schematics of the theoretical model: (**a**) and (**b**) the 2D plots of wavenumber- and time-resolved reflectance change ($\Delta R/R$) spectra with an optical pump fluence of $101\,\mu J/cm^2$ for Bi_2Te_2Se (**a**) and Sb_2TeSe_2 (**b**) single crystals. The red and green colors respectively represent the parts with a positive change and a negative change. The zero-crossing line is marked $L_{0\times}$ as a black dashed line. (**c**) shows the p-polarized reflectivity before pumping (R_p, gray solid-line. Assume N is $12.5 \times 10^{18}\,cm^{-1}$, so $\omega_p = 1880\,cm^{-1}$ with $m^* = 0.32$ and $\varepsilon_0 = 23.7$) and after pumping ($R_p{}^*$, red solid-line. Assume N is $25 \times 10^{18}\,cm^{-1}$ so $\omega_p = 2630\,cm^{-1}$ with $m^* = 0.32$ and $\varepsilon_0 = 23.7$) for the Drude model and (**d**) shows the p-polarized reflectivity before pumping (R_p, gray solid-line. Assuming $\mu = 50\,meV$ at room temperature) and after pumping ($R_p{}^*$, red solid-line. Assuming $\mu = 40\,meV$ at room temperature) for the SST-Kubo model.

Quantitative analysis of the ultra-broadband MIR $\Delta R/R$ spectra.

To quantitatively reveal the hidden mechanism, the Drude model and the SST-Kubo model are used to fit the ultra-broadband MIR $\Delta R/R$ spectra for n-type Bi_2Te_2Se and p-type Sb_2TeSe_2 TIs. It is initially assumed that before and after pumping, all reflectivity R_p (gray solid-line, before pumping) and $R_p{}^*$ (red solid-line, after pumping) have similarly shaped spectra for both the Drude model (Fig. 2c) and the SST-Kubo model (Fig. 2d). After pumping, the reflection spectrum shifts because there is an increase in the free carrier concentration. In terms of the Drude model, the dielectric function ε_D is:

$$\varepsilon_D(\omega) = \varepsilon_\infty - \frac{\omega_p^2}{\omega^2 + i\Gamma\omega} \tag{1}$$

where ε_∞ is the permittivity at an infinite frequency, ω is the frequency, ω_p is the plasma frequency and Γ is the plasma scattering rate. The carrier concentration N is related to the effective mass m^* by the equation, $N = m^*\omega_p^2/4\pi e^2$. However, Falkovsky et al. estimated the reflectivity by considering the SSTs[20]. The dielectric function using the Kubo formula is:

$$\varepsilon_F(\omega) = -\frac{8T}{(\omega^2 + i\tau^{-1}\omega) \cdot d_{TSS}}\left(\frac{e^2}{\hbar}\right)\ln\left[2\cosh\left(\frac{\mu}{2T}\right)\right]$$
$$+ \frac{1}{d_{TSS}}\left(\frac{e^2}{\hbar}\right)\left[\frac{i\pi}{\omega}G\left(\frac{\omega}{2}\right) - 4\int_0^{+\infty}d\xi\frac{G(\xi) - G\left(\frac{\omega}{2}\right)}{\omega^2 - 4\xi^2}\right] \tag{2}$$
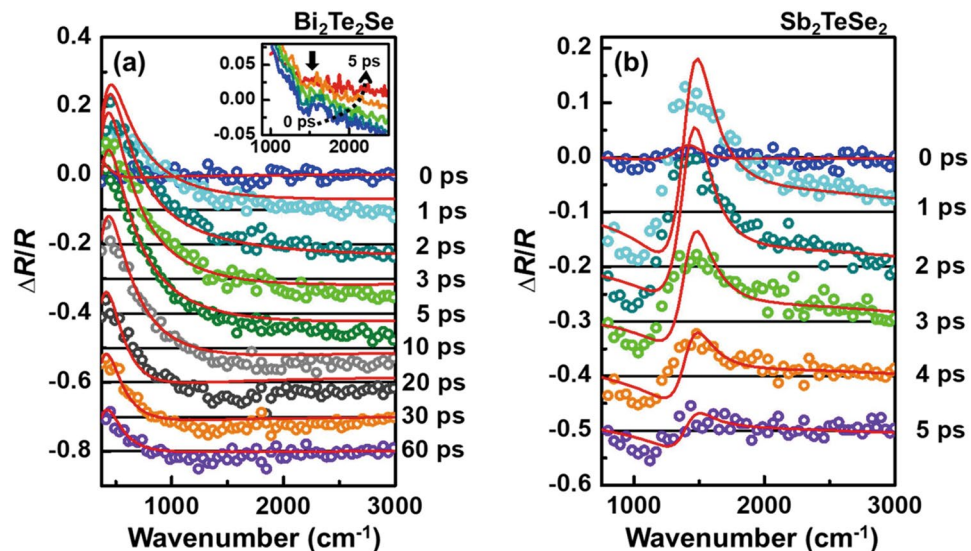
Figure 3. Typical ultra-broadband MIR $\Delta R/R$ spectra with fitting curves, taking account of free carrier absorption (FCA) and surface state transition (SST). $\Delta R/R$ as a function of the wavenumber for different delay times for (**a**) Bi_2Te_2Se and (**b**) Sb_2TeSe_2, using a pump fluence of 101 μJ/cm². The open circles represent the experimental data and each $\Delta R/R$ spectrum is shifted for clarity. The red lines are the fitting curves with **a** the Drude model and **b** the Drude-SST-Kubo model ($\delta_\omega = -690\,cm^{-1}$). The insert in a shows the Moss-Burstien shift, as indicated by the arrow. Between the top solid line and the bottom solid line are the spectra that are respectively obtained by averaging the data from 0–1 (red), 1–2 (orange), 2–3 (bright green), 3–4 (green) and 4–5 (blue) ps.

where μ is the chemical potential, T is the carrier temperature, G is the Fermi-Dirac distribution function, τ^{-1} is the collision rate for TSSs, which depends on the density of impurities, and d_{TSS} is the optical penetration depth of the TSSs. The first and second terms respectively represent the intra-band transitions and the inter-band transitions in Dirac cone. Both models are applied under the "quasi-equilibrium" state in a view of sub-10 fs probe pulse (see S2 of Supplementary information). The penetration depth of ultra-broadband MIR in TIs is few μm (see S3 of Supplementary information).

As previously mentioned, the increase of N in the Drude model represents the change in the electronic population after pumping. In Fig. 2c, the estimated value of N for R_p^* is larger than that for R_p, which results in a blue-shift in the plasma edge. In the SST-Kubo model, the photo-excitation has a significant impact on μ and T and induces changes in the reflection spectrum. In terms of the ground state of p-type Sb_2TeSe_2, both the smaller number of carriers in the vicinity of the Dirac point and the higher electron temperature result in a reduction in μ[20]. Therefore, after pumping, the reduction in the chemical potential μ causes a change in the reflection spectrum from R_p to R_p^*, as shown in Fig. 2d. This result is in good qualitative agreement with the $\Delta R/R$ spectrum in Fig. 2b.

Ultrafast time-evolution of the ultra-broadband MIR $\Delta R/R$ spectra.

Figure 3 shows the typical time-evolution of the MIR $\Delta R/R$ spectrum and the fitted curves. As mentioned previously, the photoexcited carrier dynamics in n-type Bi_2Te_2Se is dominated by FCA and can be fitted well with the Drude model, as shown in Fig. 3a. For Sb_2TeSe_2, the contribution of FCA to the photoexcited carrier dynamics cannot be neglected. Therefore, the $\Delta R/R$ spectra are fitted with the modified dielectric function of $\varepsilon_{DF}(\omega + \delta\omega) = \varepsilon_D(\omega + \delta\omega) + \varepsilon_F(\omega + \delta\omega)$, where δ_ω is a shifted frequency in fitting (This is called the Drude-SST-Kubo model). Figure 3b shows that this model fits the MIR $\Delta R/R$ spectrum at various delay times quite well. The details of the fitting are presented in the Method section.

Discussion

The fitting results in Fig. 4a,b are of interest, in particular the time evolutions of ω_p, Γ, N, μ, and T in TI's. During the pumping process, the 1.55-eV pump photons excite the electrons to a higher BCB from the occupied states[1]. For Bi_2Te_2Se, both ω_p and Γ respectively exhibit growth and relaxation dynamics. Although it is difficult to obtain the real value of N because there is no m^*, it is still possible to obtain the temporal evolution of N through $N \propto \omega_p^2$, as shown in Fig. 4c,d. The seriously shift of ω_p (~3.7 times after photo-excitation) equivalents to the dramatic enhance of photo-excited concentration (see S4 in Supplementary information). This photoexcited carrier mainly experiences FCA in bulk states (BSs), as shown by the notation of probe(1) and probe(2) in Fig. 4e, or in TSSs, as shown by the notation of probe(3). A bi-exponential decay function is further used to obtain the reduction times for the concentration of photoexcited carriers. This has a maximum within ~2.2 ps and then undergoes two relaxation processes for 1.5 ps and 8.4 ps. The fast relaxation process is caused by the thermal diffusion in BCB and TSS[27,28], or the acoustic-phono assistant process[3]. The slow one is consistent with the results of time-resolved
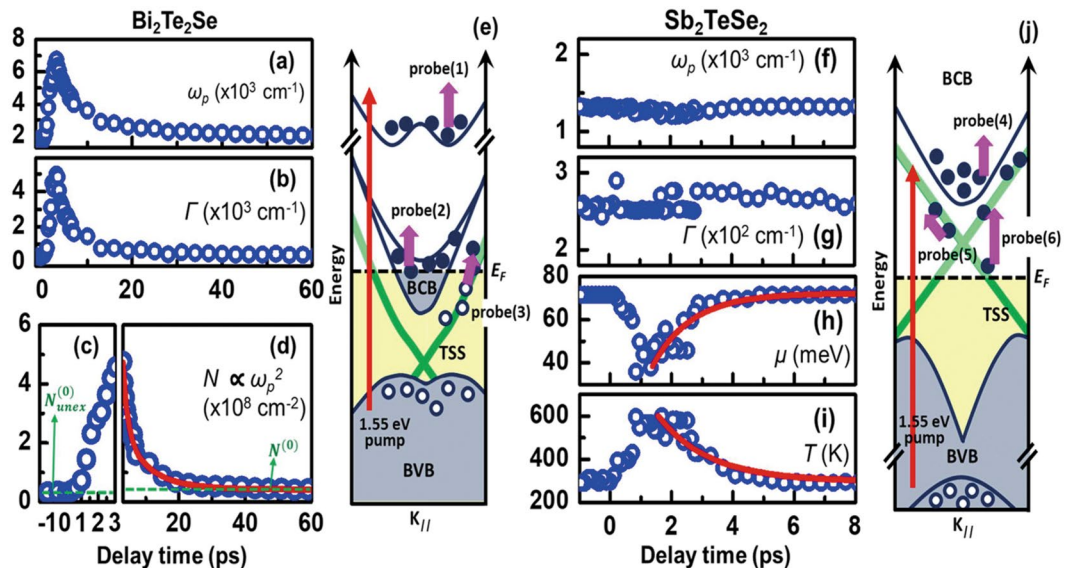
Figure 4. The time-evolution of ω_p, Γ, μ, T and the schematic energy band structure of TIs for pump/probe processes. The fitting results (**a–d**) and the pump-probe scheme (**e**) for Bi_2Te_2Se and (**f–i**) and for Sb_2TeSe_2 (**j**). (**a,b**) respectively show the time-evolution of the fitting parameter ω_p and Γ for the Drude model for a Bi_2Te_2Se crystal. (**c,d**) show the partial trace of the squared values of ω_p before **c** and after 3 ps (**d**) The red line in **d** shows the bi-exponential fitting that is described in the Method section. The green dashed lines in **c** marked by $N_{unex}^{(0)}$ ($3.42 \times 10^7\,cm^{-2}$) relate to the concentration of unexcited carriers and (**d**) marked by $N^{(0)}$ ($4.16 \times 10^7\,cm^{-2}$) represent the height of the constant term from the fitting curve. The time-domain traces for (**f**) ω_p, (**g**) Γ, (**h**) μ and (**i**) carrier temperature T are obtained using the Drude-SST-Kubo model. The red lines in (**h**), (**i**) show the single-exponential fitting that is mentioned in the Method section. The red arrows and pink arrows respectively show the 1.55 eV (800 nm) pumping and the MIR probing in (**e**), (**j**). The notation E_F in (**e**), (**j**) is the Fermi energy.

ARPES[1,2]. Additionally, the appearance of a Moss-Burstien shift (until ~6 ps) near the bulk band gap (see the inset in Fig. 3a) also indicates the recombination in BSs[15]. However, the value of N (*i.e.*, $N^{(0)}$ in Fig. 4d) does not recover to its original value (*i.e.*, $N_{unex}^{(0)}$ in Fig. 4c) within the limited delay time (~ 100 ps). This inconsistency between $N^{(0)}$ and $N_{unex}^{(0)}$ is explained by the long-lived recombination process (see S5 in Supplementary information). There are several scenarios proposed for this long relaxation process. First, it is generally assigned to the photo-voltage effect[29]. Moreover, huge Rashba-splitting effect has been clearly observed in BCB[30,31], which might cause the long-time relaxation processes like indirect band-gap semiconductors[25].

For p-type Sb_2TeSe_2, the Drude-SST-Kubo model is used to fit the results in Fig. 4f–i. It is worth emphasizing that the relative changes in μ and T are more distinct than the changes in ω_p and Γ. Even though the MIR probe-pulses can also detect FCA (even though it originates from TSSs or BSs as shown by the notation of probe(4) in Fig. 4j), the $\Delta R/R$ spectra are significantly dominated by SST's in the Dirac cone (see the notations of probe(5) and probe(6)). Figure 4h shows that after the deep valance electrons are excited to the upper Dirac cone[5], μ reaches a minimum at ~1 ps and it takes ~1.28 ps for the recombination process according to the fitting for a single exponential decay function. Besides, the hot-carrier temperature reaches ~600 K, and recovers to room temperature after 1.68 ps, which results are consistent with the time-resolved ARPES results for Sb_2Te_3[5–7]. Therefore, this hot-carrier temperature decay would be resulted from the thermal diffusion between BVB and TSS[27].

By taking account of the difference of the number of states between bulk and surface, when the electrons are photo-excited, the chemical potential should shift towards the higher energy direction. In Drude-SST-Kubo model, the chemical potential (μ) and the carrier temperature (T) are associated with the surface state, and the SST-Kubo term is consisted by inter-transition and intra-transition of Dirac cone. For $\mu \gg T$, the intra-transition term could be derived to the form[20] $\varepsilon_{F,intra} = - e^2 |\mu|/\pi\hbar(\omega^2 + i\omega\Gamma_{im})$ which coincides with the Drude expression, and the effective plasma frequency $\omega_{p,S}$ could be further expressed as $\sqrt{e^2|\mu|/\pi\hbar}$. More precisely, the contribution of excited charges to "ω_p" in Dirac cone is considered by the intra-transition term. In other words, the Drude term in Drude-SST-Kubo model represents the excited carriers which are out of the surface state. For p-type Sb_2TeSe_2 with the Fermi level locating at the lower energy part of the Dirac cone, after photoexcitation, the chemical potential shifts to the higher energy direction, and further indicates the redshift of plasma edge and decreasing of the density of states. From the fitting result of smaller ω_p (~$1.3 \times 10^3\,cm^{-1}$) on Sb_2TeSe_2, it shows the lower contribution from the excited bulk carriers, which is consistent with the results in Fig. 2b.

Summary. The ultrafast dynamics of Dirac fermions and bulk free carriers in the TIs, n-type Bi_2Te_2Se and p-type Sb_2TeSe_2 single crystals, are studied using time-resolved ultra-broadband MIR spectroscopy. The dynamics

in the n-type Bi_2Te_2Se is dominated by bulk carriers because the $\Delta R/R$ spectra show a blue-shift in the plasma edge due to FCA. For p-type Sb_2TeSe_2, the dynamics is dominated by the Dirac fermion from the red-shift of the plasma edge in the $\Delta R/R$ spectra. This study shows that the MIR absorption peaks for FCA and SST in TIs can be distinguished and demonstrates the importance of time-resolved ultra-broadband MIR spectroscopy for gapless or small band gap exotic materials.

Methods

Experimental setup.
Optical pump and ultra-broadband MIR probe spectroscopy[23] consists of three stages: (i) 800-nm optical pulses with a duration of 30 fs were generated, (ii) ultra-broadband MIR probe pulses were generated in nitrogen and (iii) chirped pulses were generated for detection. The fundamental pulses (800 nm) and the second harmonic pulses (400 nm, which were generated by a type I β-BaB_2O_4 crystal with a thickness of 0.1 mm) from a Ti:sapphire amplifier (790 nm, 30 fs, 0.85 mJ at 1 kHz, Femtopower compactPro, FEMTOLASERS) were focused into nitrogen gas to generate MIR pulses. The filamentation occurred *via* four-wave DFG when the pulse was focused using a concave mirror ($r = 1$ m). The length of the filament was ~3 cm. The bandwidth and the duration of the generated MIR pulses were 200–5000 cm^{-1} and 8.2 fs, respectively. When the MIR pulses were reflected from the sample with an incident angle of 45°, they were converted to ~400-nm pulses for the detection using a chirped-pulse up conversion (CPU) in nitrogen gas. A third 800-nm beam was transmitted through dispersive materials, including four BK7 glass plates (thickness: 10 mm) and one ZnSe plate (thickness: 5 mm), to produce chirped pulses. The converted visible (VIS) spectrum was measured by a spectrometer with an electron-multiplying CCD camera (SP-2358 and ProEM+1600, Princeton Instruments). The time resolution was estimated to be ~60 fs. To prevent significant absorption from vapor, the system was placed in boxes whose interior was purged with nitrogen.

Retrieving the MIR spectra from an up-converted spectra and calibrating the spectra of the VIS pulse to MIR region.
The MIR spectrum form, especially the sharp absorption peaks, can be seriously distorted after CPU measurements. That is to say, the dispersion of chirped pulses causes additional oscillations in the spectrum[32,33]. The CPU signal ($E_{CP}^2(t - \tau)E_{MIR}^*(t)$) was obtained by performing four-wave DFG (FWDFG, $E_{FWM}(t)$) between the chirped pulse ($E_{CP}^2(t - \tau)$) and the MIR pulse ($E_{MIR}(t)$). The chirped pulse is written as:

$$E_{CP}(t) = \mathcal{E}_{CP}(t)e^{i\omega^{(0)}t + i\frac{1}{2}\omega^{(1)}t^2} \tag{3}$$

where $\mathcal{E}_{CP}(t)$ represents the envelope, $\omega^{(0)}$ is the central angular frequency, and $\omega^{(1)}$ is a chirp parameter. The MIR pulse can be divided into a main part $E_{MIR}^{(0)}(t)$ and a free induction decay part $E_{MIR}^{(1)}(t)$. Substituting $E_{MIR}(t) = E_{MIR}^{(0)}(t) + E_{MIR}^{(0)}(t)$ yields:

$$E_{FWM}(t) = E_{CP}^2(t)E_{MIR}^{(0)*}(t) + E_{CP}^2(t)E_{MIR}^{(1)*}(t) = E_{FWM}^{(0)}(t) + E_{FWM}^{(1)}(t) \tag{4}$$

where $E_{FWM}^{(0)}(t)$ can be assumed to be the Dirac delta function $\delta(t)$ due to the short duration of MIR pulse. Using the Wiener–Khinchin theorem and these assumptions, the autocorrelation $C_A(t)$ of $E_{FWM}(t)$ is formed by[33]

$$
\begin{aligned}
C_A(t) &= \int dt' E_{FWM}^*(t')E_{FWM}(t' + t) \\
&= \delta(t) + E_{MIR}^{(1)*}(t)\mathcal{E}_{CP}^2(t)e^{i2\omega^{(0)}t + i\omega^{(1)}t^2} \\
&\quad + E_{MIR}^{(1)}(-t)\mathcal{E}_{CP}^{*2}(-t)e^{i2\omega^{(0)}t - i\omega^{(1)}t^2}
\end{aligned}
\tag{5}
$$

A similar autocorrelation form $C_A'(t)$ is obtained for a pulse that is up-converted using a monochromatic pulse by multiplying $e^{-i\omega^{(1)}t^2\text{sign}(t)}$, so that Eq. (5) becomes[33]

$$C_A'(t) = \delta(t) + E_{MIR}^{(1)*}(t)\mathcal{E}_{CP}^2(t)e^{i2\omega^{(0)}t} + E_{MIR}^{(1)}(-t)\mathcal{E}_{CP}^{*2}(-t)e^{i2\omega^{(0)}t} \tag{6}$$

Therefore, the original MIR spectrum with shift $2\omega^{(0)}t$ is acquired using the measured up-converted power spectrum and the known value of $\omega^{(1)}$ for the chirped pulse. Finally, the wavenumber is calibrated using a binomial fitting of the three absorption peaks, including carbon dioxide (~2300 cm^{-1}) and water vapor (~1600 cm^{-1} and ~3700 cm^{-1}).

Analyses using the Drude, SST-Kubo and Drude-SST-Kubo models.
In this study, the dielectric function ε in the Drude model, the SST-Kubo model and the Drude-SST-Kubo model is used to calculate the p-polarized reflectivity R_p using the Fresnel equation (with an incident angle of 45°) as:

$$R_p = \frac{\varepsilon\cos\theta - \sqrt{\varepsilon - \sin^2\theta}}{\varepsilon\cos\theta + \sqrt{\varepsilon - \sin^2\theta}} \tag{7}$$

The transient $\Delta R/R$ is obtained by:

$$\frac{\Delta R}{R} = \frac{R_p^* - R_p^0}{R_p^0} \tag{8}$$

where the superscripts "*" and "0" of R_p respectively represent the reflectivity with and without optical pumping. The fitting with the Drude model is performed using the software, RefFIT[34]. The fitting with the Drude-SST-Kubo model uses 4 parameters: ω_p, Γ, μ and T. To limit the computational load without losing the accuracy, the grid search method and an interval search algorithm with few iterations are used. After obtaining all possible values for these 4 parameters, the most appropriate parameter set P^j is selected by calculating the minimum root-mean-square deviation between the data and the calculated results at the jth iteration. More specifically, using the grid search method, the value of P^j at the jth iteration can be obtained. The best interval is decided using the neighboring points of P^j. In this analysis, 4 parameters produce the 8 neighboring points. Using this interval, the next iteration $j+1$ of the grid search is undertaken. Therefore, the accuracy is exponentially increased.

The conditions, R_p^0, are determined using the ARPES results and the FTIR spectra. For Bi_2Te_2Se, R_p^0 is calculated using the Drude model with $\varepsilon_\infty = 23.7$, $\omega_p = 1880\,cm^{-1}$ and $\Gamma = 272\,cm^{-1}$, which values are obtained by fitting the FTIR spectra using the RefFIT program[34]. For Sb_2TeSe_2, R_p^0 is determined using the Drude-SST-Kubo model with $\varepsilon_\infty = 19.4$, $\omega_p = 1320\,cm^{-1}$, $\Gamma = 253\,cm^{-1}$, $d_{TSS} = 1.4\,nm$, $\mu = 72\,meV$ and $T = 297\,K$. The former 4 parameters are obtained by fitting with fixed values of μ and T using the grid search method and an interval search algorithm, as described previously. If μ is sufficiently large, it can be estimated as:

$$\mu = \sqrt{\pi N_{TSS}}\,\hbar\upsilon_{TSS} \tag{9}$$

where N_{TSS} is the surface carrier concentration ($\sim 2.2 \times 10^{12}\,cm^{-2}$). The parameter N_{TSS} is expressed as:

$$N_{TSS} = \frac{A_{FS}}{A_{BZ}A_{UC}} = \frac{\pi K_F^2}{\left(\frac{4\pi^2}{a^2}\right)(a^2)} = \frac{K_F^2}{4\pi} \tag{10}$$

where A_{FS} is the area of the Fermi surface, A_{BZ} is the area per Brillouin zone, A_{UC} is the area per unit cell and K_F is the Fermi-wavenumber ($\sim 5.2 \times 10^6\,cm^{-1}$ from ARPES). The parameter $\upsilon_{TSS} = 4.12 \times 10^7\,cm/s$ is estimated from the gradient of Dirac cone from ARPES. More ARPES information of TIs is shown in S1 of Supplementary information.

Exponential fitting in Fig. 4.

The red line in Fig. 4d shows the bi-exponential fitting for $N^{(0)} + N^{(1)}\exp[-t/\tau_{N,1}] + N^{(2)}\exp[-t/\tau_{N,2}]$ for ω_p^2 (proportional to the time evolution of N) with a delay time t, where the parameters $N^{(0)} = 4.16 \times 10^7\,cm^{-2}$, $N^{(1)} = 1.79 \times 10^9\,cm^{-2}$, $N^{(2)} = 2.6 \times 10^8\,cm^{-2}$, $\tau_{N,1} = 1.5\,ps$, and $\tau_{N,2} = 8.4\,ps$. The red line in (h) shows the single-exponential fitting for $\mu^{(0)} + \mu^{(1)}\exp[-t/\tau_\mu]$ for the transient chemical potential $\mu(t)$, where $\mu^{(0)} = 72\,meV$ is static chemical potential, $\mu^{(1)}$ is 99 meV and $\tau_\mu = 1.28\,ps$. The red curve in Fig. 4i is fitted using a single-exponential function of $T^{(0)} + T^{(1)}\exp[-t/\tau_T]$ and the time evolution of the temperature, where $T^{(0)}$ represents the room temperature, $T^{(1)}$ is 770 K and τ_T is 1.68 ps.

References

1. Hajlaoui, M. et al. Tuning a Schottky barrier in a photoexcited topological insulator with transient Dirac cone electron-hole asymmetry. Nat. Commun. **5**, 3003 (2014).
2. Neupane, M. et al. Gigantic surface lifetime of an intrinsic topological insulator. Phys. Rev. Lett. **115**, 116801 (2015).
3. Qi, J. et al. Ultrafast carrier and phonon dynamics in Bi_2Se_3 crystals. Appl. Phys. Lett. **97**, 182102 (2010).
4. Wang, M. C., Qiao, S., Jiang, Z., Luo, S. N. & Qi, J. Unraveling photoinduced spin dynamics in the topological insulator Bi_2Se_3. Phys. Rev. Lett. **116**, 036601 (2016).
5. Sánchez-Barriga, J. et al. Ultrafast spin-polarization control of Dirac fermions in topological insulators. Phys. Rev. B **93**, 155426 (2016).
6. Zhu, S. et al. Ultrafast electron dynamics at the Dirac node of the topological insulator Sb_2Te_3. Sci. Rep. **5**, 13213 (2015).
7. Reimann, J., Gudde, J., Kuroda, K., Chulkov, E. V. & Hofer, U. Spectroscopy and dynamics of unoccupied electronic states of the topological insulators Sb_2Te_3 and Sb_2Te_2S. Phys. Rev. B. **90**, 081106(R) (2014).
8. Whitney, W. S. et al. Gate-Variable Mid-Infrared Optical Transitions in a $(Bi_{1-x}Sb_x)_2Te_3$ Topological Insulator. Nano Lett. **17**, 255–260 (2017).
9. Luo, C. W., Tseng, P. S., Chen, H.-J., Wu, K. H. & Li, L. J. Dirac fermion relaxation and energy loss rate near the Fermi surface in monolayer and multilayer graphene. Nanoscale. **6**, 8575 (2014).
10. Luo, C. W. et al. Snapshots of Dirac Fermions near the Dirac Point in Topological Insulators. Nano Lett. **13**, 5797–5802 (2013).
11. Dong, T., Yuan, R.-H., Shi, Y.-G. & Wang, N.-L. Temperature-Induced Plasma Frequency Shift in Bi2Te3 and $Cu_xBi_2Se_3$. Chin. Phys. Lett. **30**, 127801 (2013).
12. Dordevic, S. V., Wolf, M. S., Stojilovic, N., Lei, H. & Petrovic, C. Signatures of charge inhomogeneities in the infrared spectra of topological insulators Bi_2Se_3, Bi_2Te_3 and Sb_2Te_3. J. Phys.: Condens. Matter. **25**, 075501 (2013).
13. Dordevic, S. V. et al. Fano q-reversal in topological insulator Bi_2Se_3. J. Phys.: Condens. Matter. **28**, 165602 (2016).
14. Dordevic, S. V. et al. Magneto-optical effects in $Bi_{1-x}As_x$ with $x = 0.01$: Comparison with topological insulator $Bi_{1-x}Sb_x$ with $x = 0.20$. Phys. Status Solidi B. **251**, 1510–1514 (2014).
15. LaForge, A. D. et al. Optical characterization of Bi_2Se_3 in a magnetic field: Infrared evidence for magnetoelectric coupling in a topological insulator material. Phys. Rev. B. **81**, 125120 (2010).
16. Pietro, P. D. et al. Optical conductivity of bismuth-based topological insulators. Phys. Rev. B. **86**, 045439 (2012).
17. Martin, C. et al. Bulk Fermi surface and electronic properties of $Cu_{0.07}Bi_2Se_3$. Phys. Rev. B. **87**, 201201(R) (2013).
18. Reijnders, A. A. et al. Optical evidence of surface state suppression in Bi-based topological insulators. Phys. Rev. B. **89**, 075138 (2014).
19. Mak, K. F., Ju, L., Wang, F. & Heinza, T. F. Optical spectroscopy of graphene: From the far infrared to the ultraviolet. Solid State Commun. **152**, 1341–1349 (2012).
20. Falkovsky, L. A. Optical properties of graphene. J. Phys.: Conf. Ser. **129**, 012004 (2008).

21. Yao, Y. *et al*. Electrically tunable metasurface perfect absorbers for ultrathin midInfrared optical modulators. *Nano Lett.* **14**, 6526–6532 (2014).
22. Wang, Y. *et al*. Observation of ultrahigh mobility surface states in a topological crystalline insulator by infrared spectroscopy. *Nat. Commun.* **8**, 366 (2017).
23. Shirai, H., Yeh, T.-T., Nomura, Y., Luo, C.-W. & Fuji, T. Ultrabroadband midinfrared pump-probe spectroscopy using chirped-pulse up-conversion in gases. *Phys. Rev. Appl.* **3**, 051002 (2015).
24. Smith, G. D. & Palmer, R. A. In *Handbook* of *vibrational spectroscopy*, (Chalmers, J. M. & Griffiths, P. R. eds.) Vol. 1 (J. Wiley and Sons, New York, 2006).
25. Yeh, T.-T. *et al*. Ultrafast carrier dynamics in Ge by ultra-broadband mid-infrared probe spectroscopy. *Sci. Rep.* **7**, 40492 (2017).
26. Tu, C.-M. *et al*. Manifestation of a Second Dirac Surface State and Bulk Bands in THz Radiation from Topological Insulators. *Sci. Rep.* **5**, 14128 (2015).
27. Sánchez-Barriga, J. *et al*. Laser-induced persistent photovoltage on the surface of a ternary topological insulator at room temperature. *Appl. Phys. Lett.* **110**, 141605 (2017).
28. Sterzi, A. *et al*. Bulk diffusive relaxation mechanisms in optically excited topological insulators. *Phys. Rev. B.* **95**, 115431 (2017).
29. Yoshikawa, T. *et al*. photovoltage on the surface of topological insulator via optical aging. *Appl. Phys. Lett.* **112**, 192104 (2018).
30. Zhu, Z.-H. *et al*. Rashba spin-splitting control at the surface of the topological insulator Bi_2Se_3. *Phys. Rev. Lett.* **107**, 186405 (2011).
31. Zhou, B. *et al*. Controlling the carriers of topological insulators by bulk and surface doping. *Semicond. Sci. Technol.* **27**, 12 (2012).
32. Nomura, Y. *et al*. Single-shot detection of mid-infrared spectra by chirped-pulse upconversion with four-wave difference frequency generation in gases. *Opt. Express.* **21**, 18249–18254 (2013).
33. Fuji, T., Shirai, H. & Nomura, Y. Ultrabroadband mid-infrared spectroscopy with four-wave difference frequency generation. *J. Opt.* **17**, 094004 (2015).
34. Kuzmenko, A. RefFIT. http://optics.unige.ch/alexey/reffit.html, (Date of access:23/05/2012) (2016).

Acknowledgements

Author contributions

C.W.L. and T.F. proposed the project. T.F., H.S and T.T.Y. developed the experimental setup. T.T.Y. and C.Y.C. collected the raw data. T.T.Y., W.H.L. and H.S. processed the data from VIS to MIR. T.T.Y. and W.H.L. carried out the calculation for the theoretical model. R.S., F.C.C. and M.M.G. fabricated the single crystals. W.Y.T. carried out the Hall measurement. C.M.C. performed the ARPES measurements. The manuscript was written by T.T.Y. and C.W.L. with the assistance of T.K. and C.M.T. All authors edited and approved the final manuscript.

Competing interests

The authors declare no competing interests.

Additional information

Supplementary information is available for this paper at https://doi.org/10.1038/s41598-020-66720-4.

Correspondence and requests for materials should be addressed to T.-T.Y. or C.-W.L.

Reprints and permissions information is available at www.nature.com/reprints.

Publisher's note Springer Nature remains neutral with regard to jurisdictional claims in published maps and institutional affiliations.